Three-Dimensional Wake Forcing Functions Generated by a High-Speed Rotor

Robert T. Johnston[*] and Sanford Fleeter[†]
Purdue University, West Lafayette, Indiana 47907

A series of experiments are described that are directed at investigating and quantifying the inherent three-dimensionality and fundamental unsteady-flow characteristics of unsteady aerodynamic forcing functions generated by high-speed compressor rotors for application to forced response. With a midspan rotor-relative inlet Mach number of 0.6, three-component velocity and unsteady-static-pressure data defining the spanwise nature of the rotor wake are acquired and analyzed at two axial locations, in both the inlet guide vane freestream and wake regions. The slanted hot-film technique enables evaluation of the ensemble-averaged-velocity field and the rms of this ensemble-averaged velocity. Data show that the rotor-wake unsteadiness is highest in the blade wake, the vortex regions, and the casing boundary layer. A strip theory approach is used to analyze these three-dimensional data. The rotor-wake data are also correlated with empirical correlations. After Fourier decomposition of the axial and tangential velocity components, a two-dimensional vortical–potential gust splitting analysis is implemented, and the vortical and potential harmonic wake gust forcing functions are determined.

Nomenclature

A_n	=	potential disturbance nth harmonic proportionality constant
C_R	=	rotor chord
D_n	=	vortical disturbance nth harmonic proportionality constant
$\dot{k}$	=	gust wave number vector
M	=	Mach number
p	=	static-pressure perturbation
S_R	=	rotor-blade spacing
s	=	streamwise distance from rotor trailing edge
U	=	mean-absolute-velocity vector
u	=	axial-velocity perturbation
u^+	=	streamwise-velocity perturbation
v	=	tangential-velocity perturbation
v^+	=	transverse-velocity perturbation
W	=	mean-rotor-relative-velocity vector
W_{dc}	=	wake streamwise centerline-velocity defect
W_o	=	freestream streamwise velocity
w	=	perturbation-velocity vector
α_s	=	sensor yaw angle
β	=	relative flow angle
δ	=	semiwake width
ξ_d	=	downstream distance measured from rotor trailing edge at midspan
$\bar{\rho}$	=	mean density
ϕ_p	=	unsteady potential

Subscripts

cf	=	cross flow
m	=	measured
p	=	potential
v	=	vortical
r	=	radial

*Development Instrumentation Technology Manager, School of Mechanical Engineering. Member AIAA.
†McAllister Distinguished Professor, School of Mechanical Engineering. Fellow AIAA.

Introduction

TURBOMACHINE flow fields are inherently unsteady, extremely complex, highly three-dimensional, and strongly influenced by multistage effects. These features are exacerbated in advanced engines as a result of their closely spaced low-aspect-ratio blading and reduced blade numbers. Unfortunately, the blade rows of these advanced machines are highly susceptible to flow-induced vibrations, with multistage and three-dimensional interactions generating these aeromechanics problems. The flow nonuniformities generated by one blade row are temporal nonuniformities to adjacent blade rows because of their relative motion. Thus, these nonuniformities are an aerodynamic forcing function, generating unsteady forces and moments on the blading. When the frequency of these periodic flow nonuniformities coincides with a blade natural frequency, blade-fatigue failure may result, thereby compromising engine durability and life.

The design methods for predicting the aeromechanics of advanced blade rows are essentially two-dimensional, based either on time-linearized analyses, because of their computational efficiency, or on time-marching analyses, which are very powerful and quite general, but computationally very expensive. Both approaches first require a definition of the unsteady aerodynamic forcing function.

Currently used wake-forcing-function empirical or semiempirical models are based on far-wake steady-flow measurements from a single isolated airfoil row, often in an incompressible flow. Typically, experiments and the wake models developed from them have been directed at steady performance, with separate equations developed for the near and far wakes.[1,2] Majjigi and Gliebe[3] developed a linear rational model to describe wake behavior where only one equation was required for both the near- and far-wake regions. These empirical or semiempirical wake models have proven to be inadequate for application to forced-response analysis of advanced closely spaced high-speed multistage blade rows. Thus, it is necessary to investigate the fundamentals of multistage-blade-row forcing functions including multistage and three-dimensional high-speed unsteady aerodynamics.

On a fundamental basis, each harmonic or gust forcing function can be considered independently. In the reference frame of the generating airfoil row, the flow is steady with perturbations in the velocity and pressure fields due to the generated wakes and potential field. The relative motion between adjacent airfoil rows causes the spatial nonuniformity of one row to produce temporal flow fluctuations, that is, an aerodynamic forcing function, at an adjacent row. These gust forcing functions consist of two components: potential or acoustic and vortical or wake disturbances. Potential disturbances,

a result of airfoil circulation and finite airfoil thickness, extend both upstream and downstream, decaying exponentially. Vortical wake interactions occur as upstream-airfoil-row-generated wakes convect downstream and periodically interact with downstream airfoil rows due to their relative motion.

Henderson and Fleeter[4] experimentally investigated the two-dimensional vortical gust modeling assumption. Forcing functions generated by perforated plates satisfied vortical gust constraints, but those generated by loaded airfoils did not. As a result of the large unsteady static-pressure perturbations present in the airfoil wakes, they suggested that better data–theory correlation would be achieved by additionally modeling and incorporating the potential component of the gust into their forcing-function model. Manwaring and Wisler incorporated the potential component of the gust into the forcing-function model using the two-dimensional analysis method developed by Giles[5] and applied the resulting analysis to low-speed turbine and compressor research data. The measured gusts are split into vortical and potential components using only the measured unsteady-velocity data. However, Feiereisen et al.[6] determined that proper splitting of forcing-function data requires measurement of the unsteady-pressure data in addition to unsteady-velocity data. Based on this, a three-dimensional modeling technique to split forcing-function data into vortical and potential components has been developed. This was accomplished by extending current state-of-the-art two-dimensional methods to three dimensions in cylindrical coordinates and assuming incompressible flow.[7]

With regard to experimental techniques, ensemble averaging is commonly used in measurements of well-defined periodic flows such as exist in turbomachines. Although ensemble averaging is an extremely valuable data-analysis technique, understanding the unsteadiness associated with rotor wakes is critical to improving forced-response analyses. Two-dimensional vortex-street wake models have been investigated and shown to exhibit many of the instantaneous-flow features found experimentally.[8,9] If the shed vortices have considerable spanwise extent, they are a mechanism for radial fluid transport. Shed vortices with a considerable spanwise extent would also act as a significant forcing function for downstream blade rows. Clearly, additional three-dimensional wake-structure data in real and high-speed turbomachines are needed.

The fundamental components of multistage unsteady aerodynamic forcing functions are the vortical wake, the potential field, and the interaction acoustic or potential modes. However, their inherent three-dimensional and unsteady (non–ensemble averaged) flow characteristics have not been addressed with regard to forcing functions of high-speed compressor rotors, a significant industry-wide concern. These are addressed in this paper, which describes an experiment directed at investigating and quantifying the highly three-dimensional and unsteady forcing functions generated by a high-speed axial compressor rotor. Note that this research is intended to illuminate key physical phenomena and not to deduce rules of thumb for design systems. Specifically, fundamental experiments are performed, with three-component velocity and unsteady-static-pressure data acquired and analyzed to define the forcing function, both vortical and potential components, generated by the high-speed rotor for application to turbomachine forced-response design systems. These data thus provide some new understanding of the key flow phenomena and are suitable for code verification by computational fluid dynamics (CFD) researchers with all needed information presented.

These experiments were performed in the Purdue Research Axial Fan facility, composed of an inlet guide vane (IGV) row and a high-speed rotor. With a midspan rotor-relative inlet Mach number of 0.6, spanwise data defining the rotor wake are acquired with a slanted hot film and dynamic-total-pressure probes at two axial locations, in both the IGV freestream and wake regions, and are subsequently analyzed. At each axial location, data are acquired in two radial traverses, one starting in the freestream region at midspan between the IGV wakes that have passed through the rotor and the other starting in the IGV wake region at midspan. The slanted hot-film technique enables evaluation of the ensemble-averaged velocity field and the rms of this ensemble-averaged velocity. A strip-theory approach
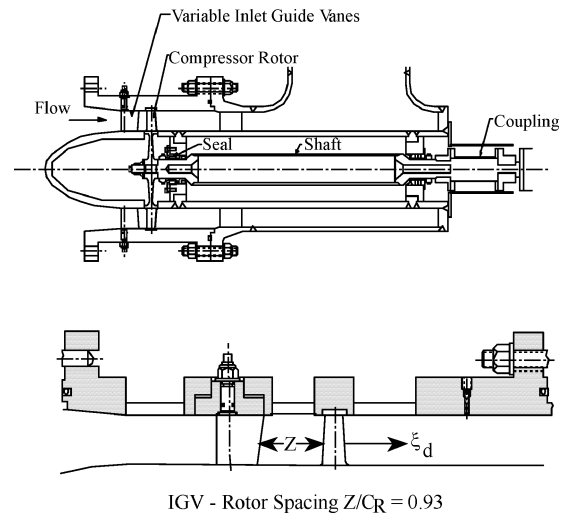

IGV - Rotor Spacing $Z/C_R = 0.93$

Fig. 1 High-speed axial fan test section.

is used to analyze these three-dimensional data. First, the rotor-wake data are correlated with empirical correlations. After Fourier decomposition of the axial and tangential velocity components, a gust-splitting analysis technique is implemented and the vortical and potential harmonic-wake-gust forcing functions are determined.

Axial Fan Facility

The Purdue Research Axial Fan Facility, composed of an IGV row and a downstream rotor, is well suited for these wake-forcing-function experiments because it is large enough for the necessary high-quality measurements, the IGV–rotor axial spacing is variable, and the IGV row can be indexed circumferentially, thereby enabling the rotor wake data to be analyzed both in the IGV freestream and in the wakes; that is, the IGV–rotor wake interactions can be investigated.

This facility features a 30.48-cm (12-in.)-diam, 2:3 hub–tip ratio design compressor rotor which is integral with the shaft. The drive system consists of a 400-hp ac motor driving a magnetic clutch with a variable speed output that drives a gearbox. Eighteen inlet guide vanes introduce swirl into a 19-blade axial-flow rotor, Fig. 1. The axial distance downstream of the rotor trailing edge is denoted by ξ_d. Both the IGVs and the rotor blades are designed with NACA 65 series airfoil sections on circular-arc meanlines. The adjustable inlet guide vanes have a nominal 10% thickness with a chord varying from 35.5 mm (1.40 in.) at the hub to 53.3 mm (2.10 in.) at the tip to yield a solidity of one. Rotor-blade sections have a 10% to 6% hub-to-tip thickness taper, with a chord of 50.8 mm (2.00 in.). Tip clearance nondimensionalized by the blade span is 1% at the leading edge. Turbulence intensity measured 26 mm upstream of the inlet guide vanes is 2.5%. For these experiments, the IGV–rotor axial spacing is $Z/C_R = 0.93$; the compressor is operated at 10,000 rpm, giving a total pressure ratio of 1.08 and a typical mass-flow rate of 3.8 kg/s (8.4 lb/s). Also, the rotor exit flowfield is axial. However, as in all real turbomachines, it is three-dimensional.

Instrumentation and Data Acquisition

Data defining the rotor wake are acquired and analyzed at two axial locations downstream of the rotor, $\xi_d/C_R = 0.08$ and 0.18, with two radial traverses from midspan. One traverse starts in the IGV freestream and the other in the IGV wake region. These are accomplished by positioning the hot film in the IGV freestream or wake region (apparent as a region with reduced mean flow velocity) at midspan and traversing radially outward. The radial traverses are made in increments of 5% blade span from midspan to 85% span and then in 2.5% span increments to the casing wall.

The unsteady-rotor-wake three-component velocity data are acquired with a slant hot-film anemometer with a measurement area of 50.8 μm $\times$ 1.0 mm. The unsteady-velocity data consist of 2000

samples taken at 500 kHz, triggered by a once-per-revolution pulse from a photo-optic sensor. The three velocity components are measured by rotating the single slant wire to four separate angles about the probe axis. Signals from the four angular positions yield four combinations of three signals. In brief, the three components of velocity are determined from the measured signals at three angular positions using a Newton–Raphson numerical technique to determine the velocity V, the yaw angle θ_y, and the pitch angle θ_p. The advantage of this method is that redundant measurements are available in the event that a particular combination fails to converge to a reasonable solution. Measurements at each probe orientation are ensemble-averaged over 200 individual revolutions and stored to disk along with the rms of the ensemble-averaged voltage signal of 2000 points. These data provide for the evaluation of the ensemble-averaged flowfield and the rms velocity of this ensemble-averaged signal. The rms velocity is determined by adding the rms voltage signal to the mean voltage, solving for the velocity with the Newton–Raphson solver, and then subtracting the mean flow velocity at that radial location. All four combinations of three rms voltage signals converge to results that are in agreement:

$$V_{\text{cf}} = (v'_\eta \hat{e}_\eta + v'_r \hat{e}_r) \qquad (1)$$

The rotor relative inlet midspan Mach number is 0.6, with a rotor absolute exit midspan Mach number below 0.3. Hence, for these rotor-wake experiments, with data acquired in the absolute reference frame, an incompressible hot-wire calibration technique is valid. Velocity calibration data are acquired with the wire oriented at 90 deg to the calibration jet and over a range of appropriate velocities. These data are analyzed to determine the coefficients A and B in the following King's law equation, which relates the wire voltage E to the effective cooling velocity V_{eff} and the thermal conductivity of air k_f:

$$E^2 = \left(B V_{\text{eff}}^{0.5} + A k_f \right)(T_w - T_f) \qquad (2)$$

Calibration data are acquired and analyzed over a range of Mach numbers from 0.1 to 0.3, over a range of pitch angles from -20 to $+20$ deg, and over yaw angles from -70 to 70 deg. The b_n coefficients in the velocity calibration,

$$V_e/V = b_0 + b_1\alpha_s + b_2\theta_p + b_3 V + b_4\alpha_s^2 + b_5\theta_p^2 + b_6 V^2$$
$$+ b_7\alpha_s\theta_p + b_8\alpha_s V + b_9\theta_p V \qquad (3)$$

are determined by a least-squares curve fit of the calibration data. A comparison of the velocity calculated from the curve fit to the calibration data yields less than 2% difference for 78% of the 758 points taken, with the remaining 22% of the data points having between 2 and 4% difference from the curve fit. These differences between the calibration data and the polynomial curve can be further reduced by selecting smaller ranges over which to fit the data, but significantly increasing the processing time required by the Newton–Raphson solver.

The unsteady static-pressure data are acquired directly with an unsteady static-pressure probe design that is insensitive to the flow velocity and yaw angle and has a high natural frequency, 60,000 kHz (Ref. 10). Some pitch sensitivity was found and accounted for during data analysis.

Wake Correlation

The rotor-blade wake decay characteristics are determined and compared with the following empirical correlations developed by Majjigi and Gliebe[3] for the semiwake width δ and the wake centerline velocity defect W_{dc}:

$$\frac{\delta}{S_R} = \frac{0.31875\,(s/C_R)\,C_D^{0.125} + 0.048}{0.268125\,(s/C_R)\,C_D^{0.125} + 1.0}$$

$$\frac{W_{\text{dc}}}{W_o} = C_D^{0.25}\,\frac{0.3675\,(s/C_R) + 1.95}{7.65\,(s/C_R) + 1.0} \qquad (4)$$

where C_R and S_R are the rotor-blade chord and spacing, s is the streamwise distance from the rotor trailing edge, C_D denotes the airfoil-section drag coefficient, and W_{dc} and W_o are the wake streamwise-velocity centerline defect and freestream streamwise velocity.

Vortical–Potential Gust Splitting Analysis

The two-dimensional inviscid flow is assumed to be compressible, isentropic, and composed of an absolute mean velocity U with superimposed small velocity w and static-pressure perturbations p. The linearized continuity and momentum equations are

$$\left(1/c_0^2\right)(\bar{D}p/Dt) + \rho \boldsymbol{\nabla} \cdot \boldsymbol{w} = 0, \qquad \bar{\rho}(\bar{D}\boldsymbol{w}/Dt) + \boldsymbol{\nabla} p = 0 \quad (5)$$

Vortical–Potential Splitting

The perturbation velocity field is split into vortical and potential gust components $\dot{w} = \dot{w}_v + \dot{w}_p$, which satisfy

$$D\boldsymbol{w}_v/Dt = 0, \qquad \boldsymbol{\nabla} \cdot \boldsymbol{w}_v = 0 \qquad (6)$$

$$\rho(D\boldsymbol{w}_p/Dt) = -\boldsymbol{\nabla} p, \qquad \left(1/\rho c_0^2\right)(\bar{D}p/Dt) = -\boldsymbol{\nabla} \cdot \boldsymbol{w}_p$$

$$\boldsymbol{\nabla} \times \boldsymbol{w}_p = 0 \qquad (7)$$

Thus, the forcing function is analyzed harmonically as a Fourier series of individual vortical and potential gusts,

$$\boldsymbol{w}(\boldsymbol{x}, t) = \sum [\boldsymbol{w}_{\text{vn}}(\boldsymbol{x}) + \boldsymbol{w}_{\text{pn}}(\boldsymbol{x})]e^{in\omega t}$$

Vortical Gust

Spatial periodicity shows that the gust wave number vector $\dot{k}$ must be perpendicular to the IGV mean-flow exit-velocity vector U:

$$\boldsymbol{k}\bar{\boldsymbol{W}} = 0 \qquad (8)$$

where $\bar{\boldsymbol{W}} = \bar{W}(\cos \beta \hat{e}_\xi + \sin \beta \hat{e}_\eta)$.

Periodicity requirements determine the tangential wave number $k_\eta = 2\pi/S_R$, with the axial wave number then determined from Eq. (8), $k_\xi = -k_\eta \tan \bar{\beta}$. The vortical gust convects with the mean flow $\bar{U}$. This condition and $\boldsymbol{\nabla} \cdot \boldsymbol{w}_v = 0$ relate the wave number vector and the gust-amplitude vector so that the gust is oriented in a direction normal to $\boldsymbol{w}_{\text{vn}}$. Combining this with Eq. (8) shows that the vortical-gust amplitude vector must be parallel to the mean velocity. Denoting the complex constant of proportionality between these two constant vectors by D_n^* leads to

$$\boldsymbol{w}_{\text{vn}} = D_n^* \bar{U} (\cos \bar{\beta} \hat{e}_\xi + \sin \bar{\beta} \hat{e}_\eta) \exp(-in\boldsymbol{k} \cdot \boldsymbol{x}) \qquad (9)$$

Thus, the vortical gust propagates unattenuated in the direction of the gust wave number vector k. This defines the vortical-gust velocity perturbation with all parameters known from measurements with the exception of D_n^*, which must be calculated for each harmonic.

Potential Gust

The potential gust $\boldsymbol{w}_p$ must satisfy $\boldsymbol{\nabla} \times \boldsymbol{w}_p = 0$ and, therefore, can be derived from a potential function, $\boldsymbol{w}_p = \boldsymbol{\nabla}\phi_p$. The perturbation potential is related to the pressure perturbation p through the unsteady Bernoulli equation. Substituting these relations into Eq. (5) yields the following perturbation-velocity potential equation:

$$\left(1/c_0^2\right)(\bar{D}/Dt)(\bar{D}\phi_p/Dt) - \boldsymbol{\nabla}^2\phi_p = 0 \qquad (10)$$

Because the flow is steady, the potential-gust solution, determined from the steady form of this equation, is

$$\phi_{\text{pn}} = A_n \exp[n(\chi k_\eta \xi - ik_\eta \eta)] \qquad (11)$$

where

$$\chi = \frac{-i M_r^2 \sin \bar{\beta} \cos \bar{\beta} \pm \sqrt{1 - M_r^2}}{1 - M_r^2 \cos^2 \bar{\beta}}$$

is the axial decay factor and A_n is a complex constant.

Thus, the potential gust is periodic in the tangential direction but decays exponentially in the axial direction. The direction of this axial decay depends on whether an upstream or downstream blade row is being analyzed. The potential static-pressure perturbation is found from the unsteady Bernoulli equation:

$$-p_{pn}/\rho\bar{U}^2 = A_n^*(-\chi\cos\bar{\beta} + i\sin\bar{\beta})\exp[n(\chi k_\eta\xi - ik_\eta\eta)] \quad (12)$$

Experimental Determination of D_n^* and A_n^*

The potential gust w_{pn} is irrotational. Therefore, the vorticity γ_{pn} is zero, $|\gamma_{pn}| = |\nabla \times w_{pn}| = 0$, and p_{pn} is given in Eq. (15). Thus, the potential gust manifests itself in both static-pressure and velocity perturbations, but not in the vorticity perturbation. The vorticity of the vortical gust is

$$|\gamma_{vn}| = |\nabla \times w_{vn}| = D_n^*\frac{ink_\eta\bar{U}}{\cos\bar{\beta}}\exp(-ink\cdot x)$$

and there is no corresponding static-pressure perturbation. Therefore, this vortical-gust component manifests itself in a vorticity perturbation, but not in a static-pressure perturbation.

The static-pressure perturbation is dependent only on the potential gust. At the measurement location $(\xi, \eta) = (0, 0)$, the potential-gust coefficient A_n^*, computed explicitly from the static pressure, is

$$A_n^* = p_{mn}/\rho\bar{U}^2(-\chi\cos\bar{\beta} + i\sin\bar{\beta}) \quad (13)$$

where p_{mn} is the measured nth harmonic static-pressure perturbation.

The potential-gust-velocity perturbation is then calculated and subtracted from the measured velocity perturbation to yield a difference velocity perturbation.[11] Because the vorticity of the potential component is zero, the perturbation of the velocity difference has the same vorticity as the measured gust. Thus the linear-theory vortical-gust coefficient is calculated from this difference-velocity perturbation as

$$D_n^* = (1/\bar{U})(u_{dn}\cos\bar{\beta} + v_{dn}\sin\bar{\beta}) \quad (14)$$

Axial and tangential unsteady-velocity components are then used to compute the streamwise and transverse components of the vortical and potential unsteady-velocity fields with the following coordinate transform:

$$\begin{pmatrix} u^+ \\ v^+ \end{pmatrix} = \begin{bmatrix} \cos\bar{\alpha} & \sin\bar{\alpha} \\ -\sin\bar{\alpha} & \cos\bar{\alpha} \end{bmatrix}\begin{pmatrix} u \\ v \end{pmatrix} \quad (15)$$

Results and Discussion

A series of experiments were performed in the Purdue Research Axial Fan Facility directed at investigating and quantifying the inherent three-dimensionality and fundamental unsteady-flow characteristics of unsteady aerodynamic forcing functions generated by high-speed compressor rotors for application to forced response. Three-component velocity and unsteady-static-pressure data defining the spanwise nature of the rotor wakes are acquired and analyzed at two axial locations, in both the IGV freestream and wake regions. First, the rotor-wake data are correlated with empirical correlations. After Fourier decomposition of the axial and tangential velocity components, a gust splitting analysis technique is implemented and the vortical and potential harmonic wake gust forcing functions are determined.

Figure 2 shows the variation with span of the rotor-exit-mass-averaged relative Mach number and flow angle, with rotor-exit-flow data presented in both the IGV wake and freestream at two axial locations. With regard to the exit relative flow angle β, there is a significant increase in β beyond 90% spanwise. Also, the slope of β is nearly constant from 50 to 90% span and from 90% span to the tip. Good agreement in the data for the various traverses is apparent. Rotor relative Mach number can be seen to be higher in the IGV freestream region at midspan. Between 65% and 80% span the traverses started in the IGV wake have higher rotor relative Mach
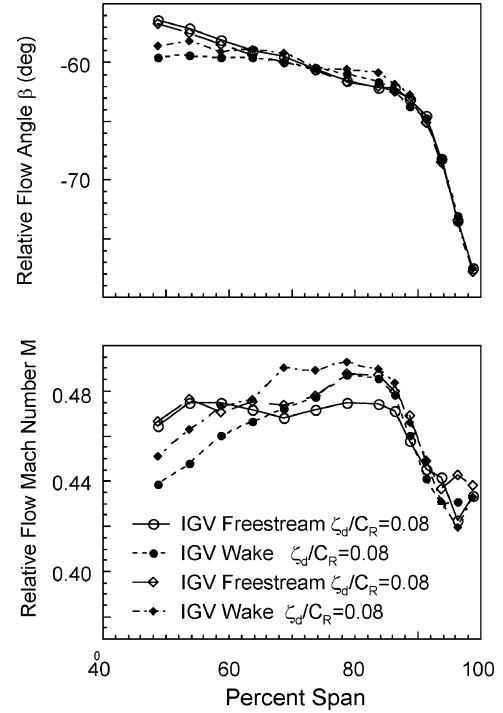

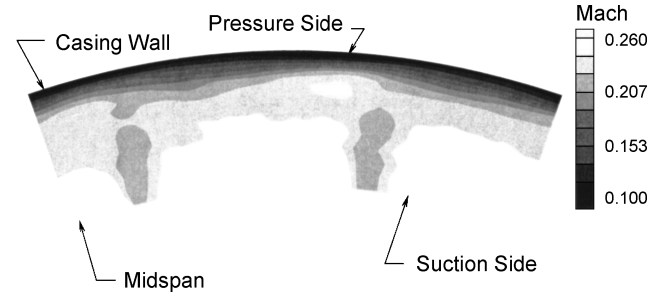**Fig. 2 Average rotor exit relative flow angle and Mach number variation with span.**

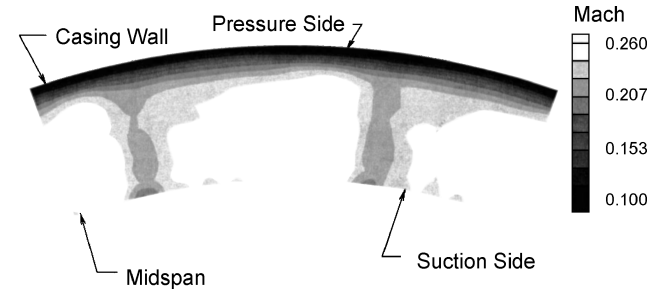**Fig. 3 Rotor-wake axial velocity in IGV freestream, $\xi_d/C_R = 0.18$.**

Fig. 4 Rotor-wake axial velocity in IGV wake, $\xi_d/C_R = 0.18$.

numbers. After 80% span, the Mach numbers for all traverses are in agreement. The rotor relative Mach number in the IGV wake nearest the rotor trailing edge is lower than that at greater axial distance, which would be expected for a decaying velocity deficit.

Rotor Exit-Velocity Field

The rotor-wake axial-velocity contours in and out of the IGV wakes at $\xi_d/C_R = 0.18$, viewed from downstream with counterclockwise rotor rotation, are presented in Figs. 3 and 4. Comparing the rotor-wake data in the IGV wake and freestream regions, the axial velocity between the rotor blades is noticeably larger in the IGV freestream region and the rotor-wake velocity deficit is larger on the
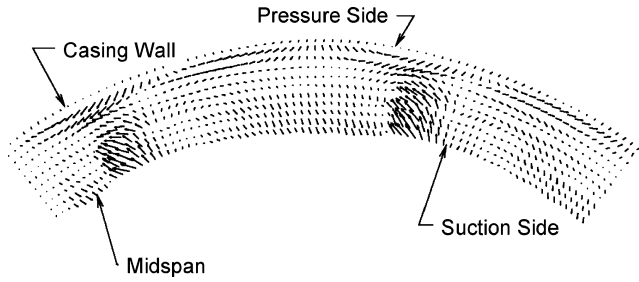
Fig. 5   Rotor-wake unsteady cross-flow velocity in IGV freestream, $\xi_d/C_R = 0.18$.
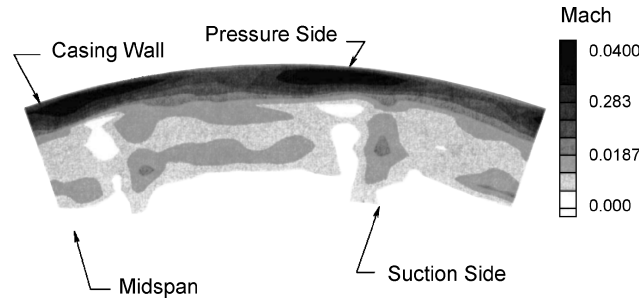

Fig. 6   RMS of ensemble-averaged rotor-wake axial velocity in IGV freestream, $\xi_d/C_R = 0.18$.

rotor-blade suction side in the IGV wake region. Also, a region of higher velocity is evident on the rotor-blade pressure side at 70% span, which is attributed to the tip-vortex flowfield.

The unsteady cross-flow velocity, derived from the rotor-wake unsteady radial and tangential velocities, derived from the unsteady radial- and tangential-velocity data, are shown in Fig. 5. Note that these rotor-wake data were acquired in the IGV freestream region but that similar results are obtained in the IGV wake regions. A vortex is apparent on the rotor-blade pressure side, possibly a combination of a clearance vortex that has migrated across the blade passage and a scraping vortex. The scraping vortex is due to the relative motion between the blade tip and the casing wall, whereas the clearance vortex forms when flow moves from the pressure side to the suction side of the blade through the tip gap. With the measurement plane parallel to the rotor-rotation plane and because it is unlikely that the tip vortex would follow an axial flow path, the vortex region appears elongated in this figure. Also, a saddle point is apparent on the rotor-blade suction side.

Figure 6 presents the rms ensemble-averaged rotor-wake axial velocity in the IGV freestream. The rotor-wake and blade-pressure-side tip regions have the highest unsteadiness levels, indicated by the large rms values. Near the casing wall, the high unsteadiness is due not only to the presence of the clearance and scrapping vortices, but also to the inherent unsteadiness in the wall boundary layer coupled with its effect on the rotor-blade aerodynamics.

Rotor-Wake Correlations

The rotor-wake semiwake width and wake centerline velocity-deficit data, in both the IGV wake and freestream regions, are compared with the empirical Majjigi–Gliebe correlations as a function of span in Figs. 7 and 8. The semiwake width data in the IGV wake and freestream are in good agreement. Also, the experimentally determined semiwake widths are larger than predicted by the correlation at all span locations. The largest deviations are between 85% span and the casing wall, where the increasing semiwake width is characteristic of flow in the tip region.

The measured velocity deficit is smaller than that predicted by the Majjigi–Gliebe correlation at all span locations, with the largest differences from 75 to 85% span. The midspan rotor-velocity deficit is smaller in the IGV wake than in the IGV freestream. However, this is reversed beyond 75% span, with the rotor velocity deficit in the IGV wake now larger than that in the IGV freestream. The
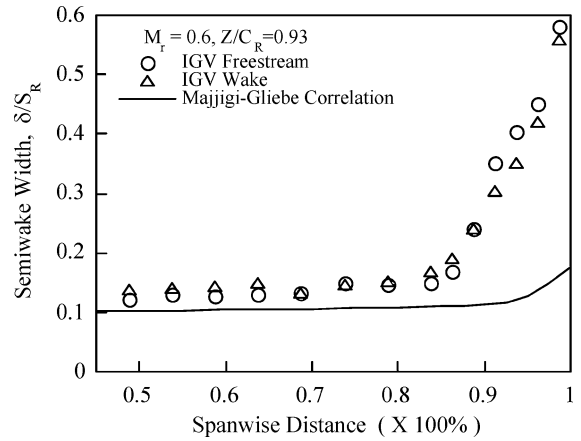

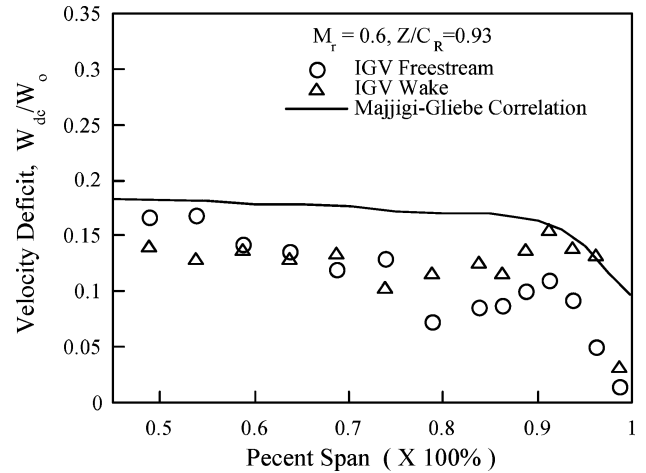**Fig. 7   Semiwake width variation with span location, $\xi_d/C_R = 0.18$.**

Fig. 8   Velocity-deficit variation with span, $\xi_d/C_R = 0.18$.

wake velocity-deficit decrease from 75 to 95% span is expected in the tip region due to the rollup of the tip vortex. Also, the local velocity-deficit maximum at 95% span is attributed to the mean relative flow-velocity reduction in the casing-wall boundary layer.

Vortical–Potential Gusts

Figure 9 shows the measured rotor-wake gust perturbation velocity vectors and static pressure, both the total profile and the first harmonic, at 50 and 95% span. The gust wave number vector is perpendicular to the rotor relative mean flow. Thus, the gust plots are constructed along a line perpendicular to the relative mean flow. Also, because the nondimensionalized velocity vectors are larger where the mean flow velocity is decreased, the scale for the 50% span data is twice that of the 95% span data.

At 50% span, the narrow viscous rotor-blade wakes are clearly visible, with the unsteady static-pressure perturbation, positive pressure to the left, small in comparison to the unsteady velocity perturbation. Also, the magnitude and phase of the first harmonic streamwise-to-transverse gust component ratio u_m^+/v_m^+ are 1.06 and 160.9 deg. Hence, the unsteady velocity vector traces out a highly eccentric ellipse[11] characteristic of a predominantly vortical flow, which rotates counterclockwise with time.

In contrast, at 95% span, the viscous wakes are not apparent, with the unsteady static-pressure perturbation quite large in comparison to the unsteady velocity perturbation. The magnitude and phase of the first harmonic streamwise-to-transverse gust component ratio u_m^+/v_m^+ are 0.5 and −32.2 deg. Thus the unsteady velocity vector traces out an almost perfect ellipse and rotates clockwise with time.

The perturbation vortical and potential components of the measured rotor-wake gust velocity vectors and static pressure at 50 and 95% span are determined by applying the splitting analysis to the
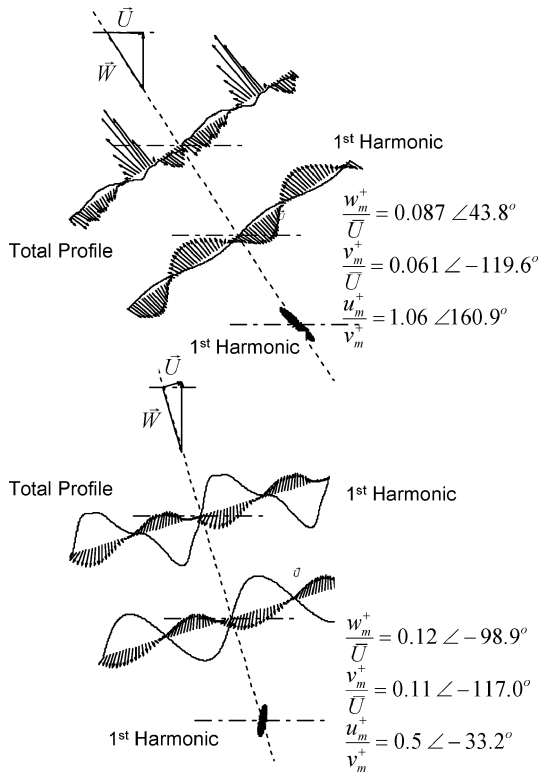
$$\frac{w_m^+}{\overline{U}} = 0.087 \angle 43.8^o$$

$$\frac{v_m^+}{\overline{U}} = 0.061 \angle -119.6^o$$

$$\frac{u_m^+}{v_m^+} = 1.06 \angle 160.9^o$$

$$\frac{w_m^+}{\overline{U}} = 0.12 \angle -98.9^o$$

$$\frac{v_m^+}{\overline{U}} = 0.11 \angle -117.0^o$$

$$\frac{u_m^+}{v_m^+} = 0.5 \angle -33.2^o$$

Fig. 9   Rotor-blade-wake gust velocity and static pressure at 50 and 95% span, $\xi_d/C_R = 0.18$.

$$A_1^* = 0.018 \angle 156^o \qquad D_1^* = 0.094 \angle 56.8^o$$
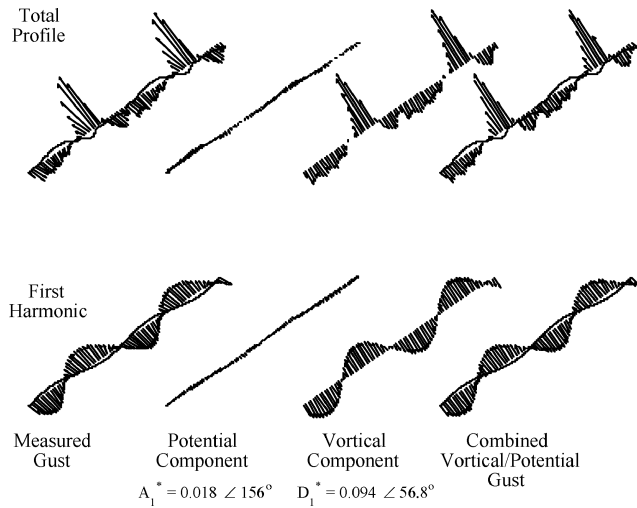
Fig. 10   Splitting analysis applied to rotor-wake gust at 50% span, $\xi_d/C_R = 0.18$.

data of Fig. 9. At 50% span, the gust is predominantly vortical, with the velocity fluctuations much larger than the static-pressure fluctuations (Fig. 10). Also, the first harmonics of the measured gust, potential components, and vortical components do not correspond to the total profiles, indicating that there is a considerable contribution from higher harmonics.

At 95% span, in contrast, the gust is predominantly potential in nature, evidenced by the large unsteady static-pressure perturbation (Fig. 11). Also, there is little contribution from higher harmonics, indicated by the total profile data being well represented by the first harmonics. Note that the ability of the splitting analysis to reconstruct the measured wake near the casing wall is hampered by the highly three-dimensional nature of the flow.

Figures 12 and 13 show the spanwise behavior of the magnitude of the rotor-wake first-harmonic potential- and vortical-gust com-
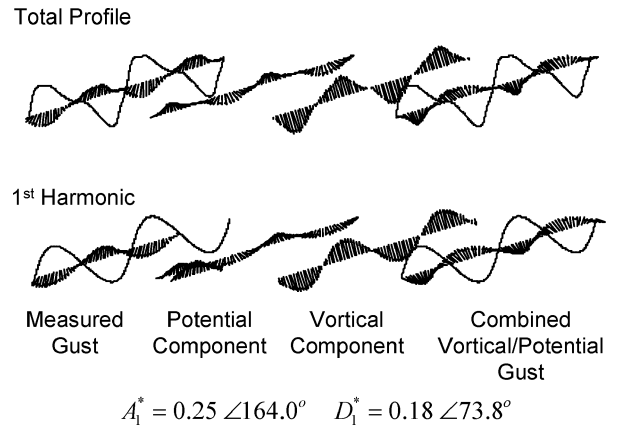

$$A_1^* = 0.25 \angle 164.0^o \qquad D_1^* = 0.18 \angle 73.8^o$$

Fig. 11   Splitting analysis applied to rotor-wake gust at 95% span, $\xi_d/C_R = 0.18$.
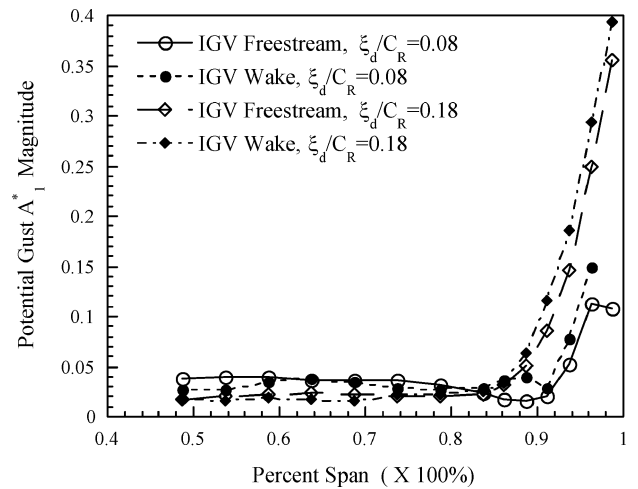

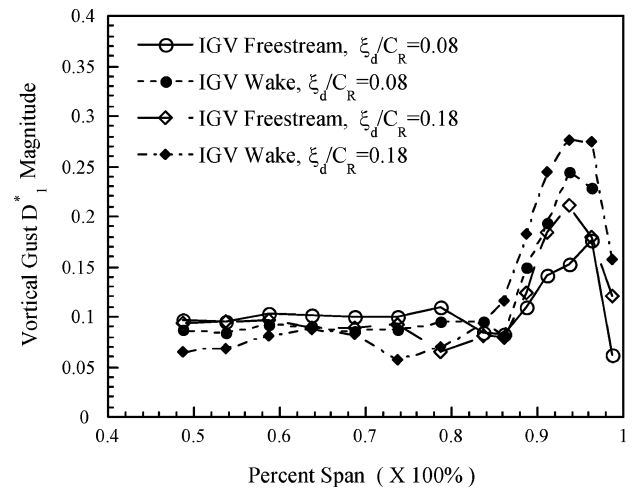**Fig. 12   First-harmonic potential-gust magnitude variation with span.**

Fig. 13   First-harmonic vortical-gust magnitude variation with span.

ponents, A_1^* and D_1^*, at two axial positions, both in the IGV wake and freestream.

In the midspan region, approximately 50 to 85% span, the potential-gust A_1^* magnitude is relatively constant, with A_1^* somewhat larger at the axial location nearer to the trailing edge of the rotor blade, as expected. Also, there is minimal effect of being in the IGV wake or freestream on these data. For span locations larger than 85%, the magnitude of A_1^* increases dramatically as the outer casing is approached. In this region, the magnitude of A_1^* is noticeably
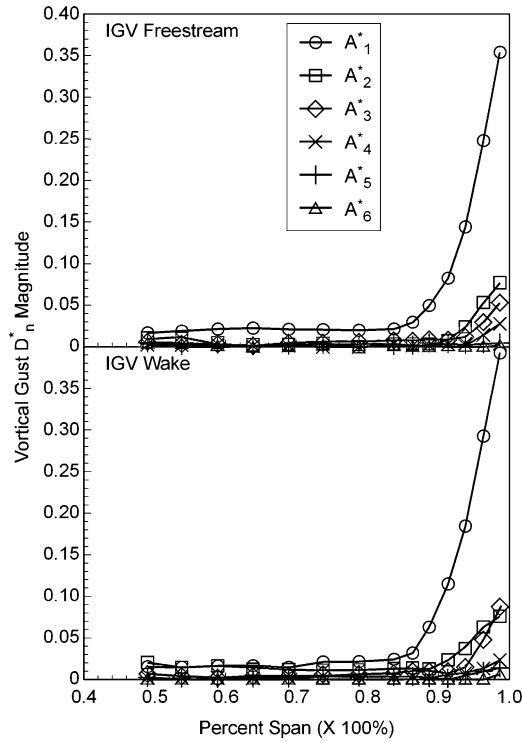
Fig. 14 Harmonics of rotor wake potential component ($\xi_d/C_R = 0.18$).

Fig. 15 Harmonics of rotor wake vortical component ($\xi_d/C_R = 0.18$).

smaller at the axial location nearer to the trailing edge of the rotor blade. Also, at both downstream positions, A_1^* has a great magnitude in the IGV wake than in the IGV freestream when the spanwise location is greater than 50%.

The magnitude of the vortical gust component D_1^* is also relatively constant in the midspan region, approximately 50 to 85% span, with a small decrease evident between 75 and 85% span. There is minimal effect of downstream position on D_1^* when the rotor wake is in the IGV freestream. However, with the rotor in the IGV wake, the magnitude of D_1^* is decreased, with the smallest value of D_1^* generally farthest from the rotor trailing edge. For span locations greater than 85%, there is a dramatic increase in the magnitude of D_1^*, analogous to the results for the potential-gust magnitude. However, there is a significant decrease in D_1^* between 95% span and the outer casing. In this outer span region beyond 85% span, the magnitude of the vortical gust is larger in the IGV wake than in the IGV freestream, with the D_1^* magnitude data smaller nearer to the rotor trailing edge.

The higher harmonics of the magnitudes of the rotor-blade wake potential- and vortical-gust components A_n^* and D_n^*, including spanwise variations and the effect of the rotor blade being in the wake or freestream regions of the IGV row, are considered in Figs. 14 and 15.

In the midspan region from approximately 50 to 85% span, the magnitudes of the rotor-blade wake potential-gust harmonics A_n^* are small. The magnitudes of the first two harmonics of the potential gust are larger in the IGV wake at midspan, as expected. That is, the IGV wake-cutting effect causes larger rotor-blade surface-pressure fluctuations, which contributes to the potential perturbation. In the outer span region beyond 85% span, all six potential gust harmonics increase, with the lower harmonics exhibiting the largest increases in magnitude. The magnitude of the first harmonic is larger in the IGV freestream than in the IGV wake. However, there is minimal effect of the IGV wake or freestream on the magnitudes of the higher potential-gust harmonics in this outer span region.

In the midspan region from approximately 50 to 85% span, the magnitudes of the rotor-blade wake vortical-gust harmonics D_n^* are all larger than the corresponding potential-gust values, with the lower harmonics having the largest differences. The first harmonic of the vortical gust component is higher for the traverse in the IGV freestream from midspan to 70% span. The unsteadiness of the IGV wake contributes to earlier blade separation, reducing vorticity shed
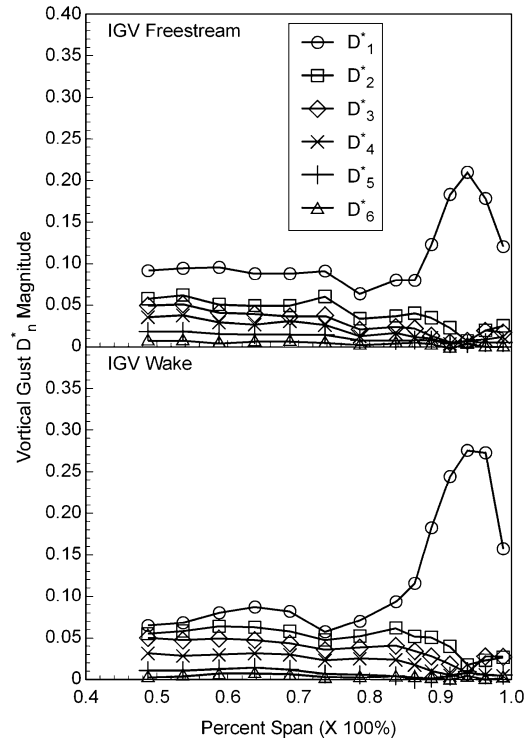
in the wake; therefore the vortical component of the rotor-blade wake in the IGV wake is reduced. The magnitude of D_n^* is relatively constant, with a local minimum evident. In the IGV wake region, this local minimum is near 75% span, whereas this minimum occurs at 80% span in the IGV freestream. In the outer span region the vortical-gust first-harmonic magnitude rapidly increases and then sharply decreases at approximately 95% span. With regard to the higher harmonics in this outer span region, after the local minimum, the higher order harmonic magnitudes all decrease with span, but then increase at 95% span as the outer casing is approached. The IGV wake and freestream have a large effect on the downstream rotor-blade wake first-harmonic vortical-gust magnitudes. The maximum value of the first-harmonic magnitude in the outer span region is larger in the IGV wake.

Summary

A series of experiments were performed directed at investigating and quantifying the inherent three-dimensionality and fundamental unsteady-flow characteristics of unsteady aerodynamic forcing functions generated by high-speed compressor rotors for application to forced response. Performed in the Purdue Research Axial Fan facility, composed of an IGV row and a high-speed rotor, three-component velocity and unsteady static-pressure spanwise data defining the rotor wake were acquired and analyzed at two axial locations, in both the IGV freestream and wake regions. The rotor-wake data were correlated with empirical correlations. Then, after Fourier decomposition of the axial and tangential velocity components, a gust-splitting analysis technique was implemented and the vortical and potential harmonic wake gust-forcing functions were determined.

The cross-flow velocity data revealed that the flow was radially outward in the rotor-blade wake from 50 to 85% span. Also, there was a vortex near the rotor-blade pressure side due to the relative motion between the rotor blade and the casing wall and the migration of the clearance vortex from the preceding blade.

The rms velocity data showed that the rotor-wake unsteadiness is highest in the blade wake, the vortex regions, and the casing boundary layer, with the largest unsteadiness in the region adjacent to the casing wall. This was attributed to the combination of the tip vortex flow and the casing-wall boundary layer.

Characteristics of the rotor-blade wakes were compared to the Majjigi and Gliebe empirical correlations, with spanwise variations considered using a strip approach. The semiwake width and velocity-deficit data and empirical correlation showed some agreement, although the semiwake width was significantly larger in the tip region and the wake deficit smaller near 75% span than predicted by the correlations.

After Fourier decomposition of the axial and tangential velocity components, a two-dimensional vortical–potential gust splitting analysis was implemented, and the vortical and potential harmonic wake gust forcing functions were determined. The potential and vortical gust components were dominated by the first harmonic component in the outer span region. Also, the higher vortical- and potential-gust harmonics were significantly reduced in the IGV wake regions.

Acknowledgment

References

[1] Ravindranath, A., and Lakshminarayana, B., "Mean Velocity and Decay Characteristics of the Near and Far-Wake of a Compressor Rotor Blade of Moderate Loading," *Journal of Engineering for Power*, Vol. 102, No. 3, July 1980, pp. 535–548.

[2] Lakshminarayana, B., and Davino, R., "Mean Velocity and Decay Characteristics of the Guide Vane and Stator Blade Wake of an Axial Flow Compressor," *Journal of Engineering for Power*, Vol. 102, Jan. 1980, pp. 50–60.

[3] Majjigi, R. K., and Gliebe, P. R., "Development of a Rotor Wake/Vortex Model, Vol. 1—Final Report," NASA CR 174849, 1984.

[4] Henderson, G. H., and Fleeter, S., "Forcing Function Effects on Unsteady Aerodynamic Gust Response, Part 1: Forcing Functions," *Journal of Turbomachinery*, Vol. 115, No. 4, 1992, pp. 741–750.

[5] Manwaring, S. R., and Wisler, D. C., "Unsteady Aerodynamics and Gust Response in Compressors and Turbines," *Journal of Turbomachinery*, Vol. 115, No. 4, 1993, pp. 724–740.

[6] Feiereisen, J. M., Montgomery, M. D., and Fleeter, S., "Unsteady Aerodynamic Forcing Functions: A Comparison Between Linear Theory and Experiment," American Society of Mechanical Engineers, ASME Paper 93-GT-141, 1993.

[7] Johnston, D. A., and Fleeter, S., "3D Turbine Rotor Forcing Functions and Linear Theory Analysis," *Journal of Propulsion and Power*, Vol. 14, No. 2, 1998, pp. 183–190.

[8] Epstein, A. H., Gertz, J. B., Owen, P. R., and Giles, M. B., "Vortex Shedding in High-Speed Compressor Blade Wakes," *Journal of Propulsion*, Vol. 4, No. 3, 1988, pp. 236–244.

[9] Capece, V. R., and Fleeter, S., "Measurement and Analysis of Unsteady Flow Structures in Rotor Blade Wakes," *Experiments in Fluids*, No. 7, No. 1, 1989, pp. 61–67.

[10] Kerrebrock, J. L., "The M.I.T. Blowdown Compressor Facility," Gas Turbine Lab., Rept. 108, Massachusetts Inst. of Technology, Cambridge, MA, May 1972.

[11] Johnston, R. T., Feiereisen, J. M., and Fleeter, S., "Rotor Wake and Potential Forcing Functions, Including Blade Row Interactions," *Journal of Propulsion and Power*, Vol. 14, No. 2, 1998, pp. 191–198.